Check for updates

ADVANCED OPTICAL MATERIALS
www.advopticalmat.de

Mid-Infrared Intersubband Transitions in *p*-Type SiGe Parabolic Quantum Wells

Marco Faverzani, Davide Impelluso, Stefano Calcaterra, Carlo Zucchetti, Daniel Chrastina, Camillo Tassi, Giovanni Capellini, Paolo Biagioni, Giovanni Isella, Michele Virgilio, and Jacopo Frigerio*

The design, fabrication, and comprehensive characterization of hole-doped Ge-rich SiGe parabolic quantum wells engineered to exhibit intersubband transitions in the mid-infrared spectral range around 120 meV are reported. The heterostructures are grown on Si substrates by low-energy plasma-enhanced chemical vapor deposition, enabling finely controlled compositional profiles and high crystalline quality. Thorough structural analysis confirms the formation of parabolic potential wells despite the presence of entropic interdiffusion. Photoreflectance spectroscopy is employed to investigate interband optical transitions in these heterostructures, whereas intersubband transitions are studied by Fourier-transform infrared spectroscopy that revealed characteristic constant-energy TM-polarized absorption features up to room temperature. At higher doping levels, a more structured spectral response is observed due to valence-band non-parabolicity. Tight-binding band structure simulations, incorporating many-body effects, accurately reproduce the observed spectral features. These results highlight the potential of SiGe parabolic quantum wells as a versatile and scalable platform for the development of Si-compatible mid-infrared optoelectronic devices based on intersubband transitions.

1. Introduction

The ability of generating, manipulating, and detecting mid-infrared (MIR) light (from 3 to 15 μm wavelength) is essential in several applications including material identification,[1] sensing,[2,3] and imaging.[4] In this context, group-IV semiconductors are currently being considered as a cost-effective and compact alternative to available commercial devices based on III–V semiconductors. Moreover, Si-compatible materials may also be monolithically integrated into the Ge-rich SiGe-on-Si material platform, which has demonstrated its potential for the realization of MIR photonic integrated circuits (PICs)[5] thanks to its wide transparency window ranging from 3 to 15 μm.

Semiconductor quantum wells (QWs) are widely employed for the implementation of infrared-active optoelectronic devices as they offer the possibility of tuning their optical response by suitably engineering the lattice strain and compositional profile. In particular, intersubband (ISB) transitions, i.e., electronic transitions that involve two confined energy levels originating from the same band, can cover both the MIR and far-infrared (FIR), down to the THz spectral region. Electrons in Si- and Ge-rich n-type SiGe QWs mainly populate the Δ or L valleys of the conduction band, respectively. In the latter case, the relatively small band-offset (100 ÷ 150 meV) only allows for ISB transitions occurring in the FIR.[6,7] Instead, hole-doped SiGe QWs can benefit from larger band-offsets that can exceed 300 meV. While *p*-type Si-rich SiGe QWs have been extensively investigated,[8,9] *p*-type Ge-rich SiGe QWs have only recently garnered attention owing to their potential application in PICs as non-linear optical components relying on their giant non-linear susceptibility,[10] electro-optic modulators exploiting the quantum-confined Stark effect,[11] and QW infrared photodetectors (QWIPs). Moreover, ISB transitions in semiconductor QWs provide a versatile platform to reach the strong light–matter coupling regime, where the interaction strength can be controlled through the carrier density. While this phenomenon has been extensively studied in III–V systems, it was only recently investigated in group-IV-based heterostructures.[12,13]

M. Faverzani, D. Impelluso, S. Calcaterra, C. Zucchetti, D. Chrastina, P. Biagioni, G. Isella, J. Frigerio
Dipartimento di Fisica
Politecnico di Milano
Piazza L. da Vinci 32, Milano 20133, Italy
E-mail: marco.faverzani@polimi.it

C. Tassi, M. Virgilio
Dipartimento di Fisica "E. Fermi"
Università di Pisa
Largo Pontecorvo 3, Pisa 56127, Italy

G. Capellini
Dipartimento di Scienze
Università degli Studi Roma Tre
Viale G. Marconi 446, Roma 00146, Italy

G. Capellini
IHP - Leibniz Institute for High Performance Microelectronics
Im Technologiepark 25, 15236 Frankfurt (Oder), Germany

The ORCID identification number(s) for the author(s) of this article can be found under https://doi.org/10.1002/adom.202503060

© 2025 The Author(s). Advanced Optical Materials published by Wiley-VCH GmbH. This is an open access article under the terms of the Creative Commons Attribution License, which permits use, distribution and reproduction in any medium, provided the original work is properly cited.

DOI: 10.1002/adom.202503060

© 2025 The Author(s). Advanced Optical Materials published by Wiley-VCH GmbH

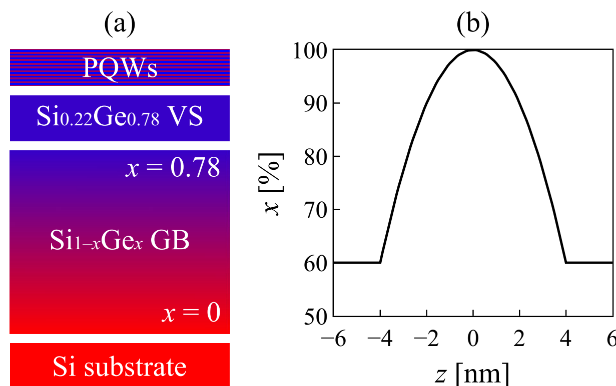

Figure 1. a) Schematic of the sample structure showing the whole stack, including the silicon substrate, the GB, the VS, and the QWs. b) Nominal Ge content profile of each PQW.

Among the possible QW designs, those exhibiting a parabolic variation of the compositional profile display the remarkable property of featuring ISB transitions whose energy is not affected by electron–electron interaction. Therefore, the transition energies are almost doping-independent,[14] making them ideal candidates for the investigation of the ISB strong coupling regime up to room-temperature. Moreover, parabolic QWs (PQWs) have been proposed for the realization of low-dark-current QWIPs.[15] However, the growth of high-quality PQWs is rather challenging, with the harmonic potential often having been approximated by digital alloying;[16] continuously-graded PQWs, instead, were only recently demonstrated, both in III–V[17,18] and SiGe[6,7,19] compound semiconductors, paving the way for their exploitation in strongly coupled systems working in the THz spectral region.[13,20] On the contrary, MIR-active PQWs are still missing. In this work, we report on the design, growth, structural, and optical characterization of hole-doped Ge-rich SiGe PQWs featuring ISB transitions at energies around 120 meV (10 µm wavelength).

2. Design and Growth

The samples were grown by low-energy plasma-enhanced chemical vapor deposition (LEPECVD)[21] on silicon substrates. With the aim of reducing the impact of threading dislocations,[22] an 11 µm-thick $Si_{1-x}Ge_x$ graded buffer (GB), where the germanium content increases at a constant grading rate of 7%/µm, was first deposited, followed by a 2 µm-thick $Si_{0.22}Ge_{0.78}$ virtual substrate (VS), as pictorially shown in **Figure 1**a. The VS composition was selected to match the average Ge content of the heterostructure and avoid plastic relaxation during the growth of the QW stack. The compositional profile was designed by means of an advanced semiempirical tight-binding model with the aim of confining at least two subband energy levels originating from the heavy-hole (HH) band. As reported in Figure 1b, each period nominally features an 8 nm-thick $Si_{1-x}Ge_x$ parabolic well, with the germanium content varying between 60 and 100 %, enclosed between 4 nm-thick $Si_{0.4}Ge_{0.6}$ barriers. As a consequence, the Ge-rich central region of each well experiences biaxial compressive strain, which removes the degeneracy between the HH and light-hole (LH) bands at Γ and promotes HH as the ground state of the system. Conversely, biaxial tensile strain occurs in the outermost regions and barriers.

Five samples were grown for the characterization of the structural and optical properties of the heterostructure. Sample A was grown to investigate the structural properties of the system and it was doped by adding a 0.1 sccm flux of B_2H_6 in the central 2 nm of the wells. Sample B was grown for the photoreflectance (PR) study of interband optical transitions, therefore it was not intentionally doped. Samples C, D and E were grown to investigate ISB transitions in such heterostructures and in particular their dependence on doping: hence, sample C was doped adding a 0.1 sccm flux of B_2H_6 in the central 2 nm, sample D adding a 0.1 sccm flux of B_2H_6 in the central 4 nm and sample E adding a 0.5 sccm flux of B_2H_6 in the central 2 nm. The relevant parameters of the investigated samples are listed in **Table 1**.

3. Structural Characterization

The structural properties of the heterostructure were investigated at the atomic scale by secondary ion mass spectroscopy (SIMS), scanning transmission electron microscopy (STEM), and energy-dispersive X-ray (EDX) spectroscopy. A STEM image of sample A is reported in **Figure 2**a: starting from the silicon substrate, on the left, the GB initially presents a large number of line defects, i.e., dislocations, which are progressively accommodated as the germanium content increases; eventually a high-quality constant-composition layer is achieved which serves as VS for the heterostructure, which is found in the rightmost part of the image. Figure 2b shows a detailed STEM image focusing on the QWs region and the corresponding EDX intensity maps of Ge and Si together with the EDX compositional profiles. With respect to the nominal design, the STEM-EDX profile, shown in Figure 2c, reveals that, on one side, the alloy composition does not reach pure germanium at the QWs center while, on the other side, the abrupt shape variation, nominally occurring at the interfaces between barriers and wells, is smoothed out. Since silicon and germanium are miscible over the entire compositional range,[23] both these effects can be ascribed to the entropic interdiffusion typical of random alloys such as silicon-germanium. Nevertheless, a parabolic variation of the germanium content was observed in the wells.

Table 1. Sample list including number of periods, XRD periodicity, doping protocol, and sheet hole density retrieved from low-temperature FTIR measurements.

Sample	Number of periods	XRD period [nm]	Doping protocol	FTIR hole density at 10 K [cm^{-2}]
A	50	12.7	0.1 sccm B_2H_6 in 2 nm	–
B	20	12.3	–	–
C	20	12.2	0.1 sccm B_2H_6 in 2 nm	7.3×10^{11}
D	20	12.4	0.1 sccm B_2H_6 in 4 nm	1.2×10^{12}
E	20	12.3	0.5 sccm B_2H_6 in 2 nm	3.6×10^{12}

© 2025 The Author(s). Advanced Optical Materials published by Wiley-VCH GmbH

21951071, 0, Downloaded from https://advanced.onlinelibrary.wiley.com/doi/10.1002/adom.202503060 by POLITECNICO DI MILANO, Wiley Online Library on [09/01/2026]. See the Terms and Conditions (https://onlinelibrary.wiley.com/terms-and-conditions) on Wiley Online Library for rules of use; OA articles are governed by the applicable Creative Commons License

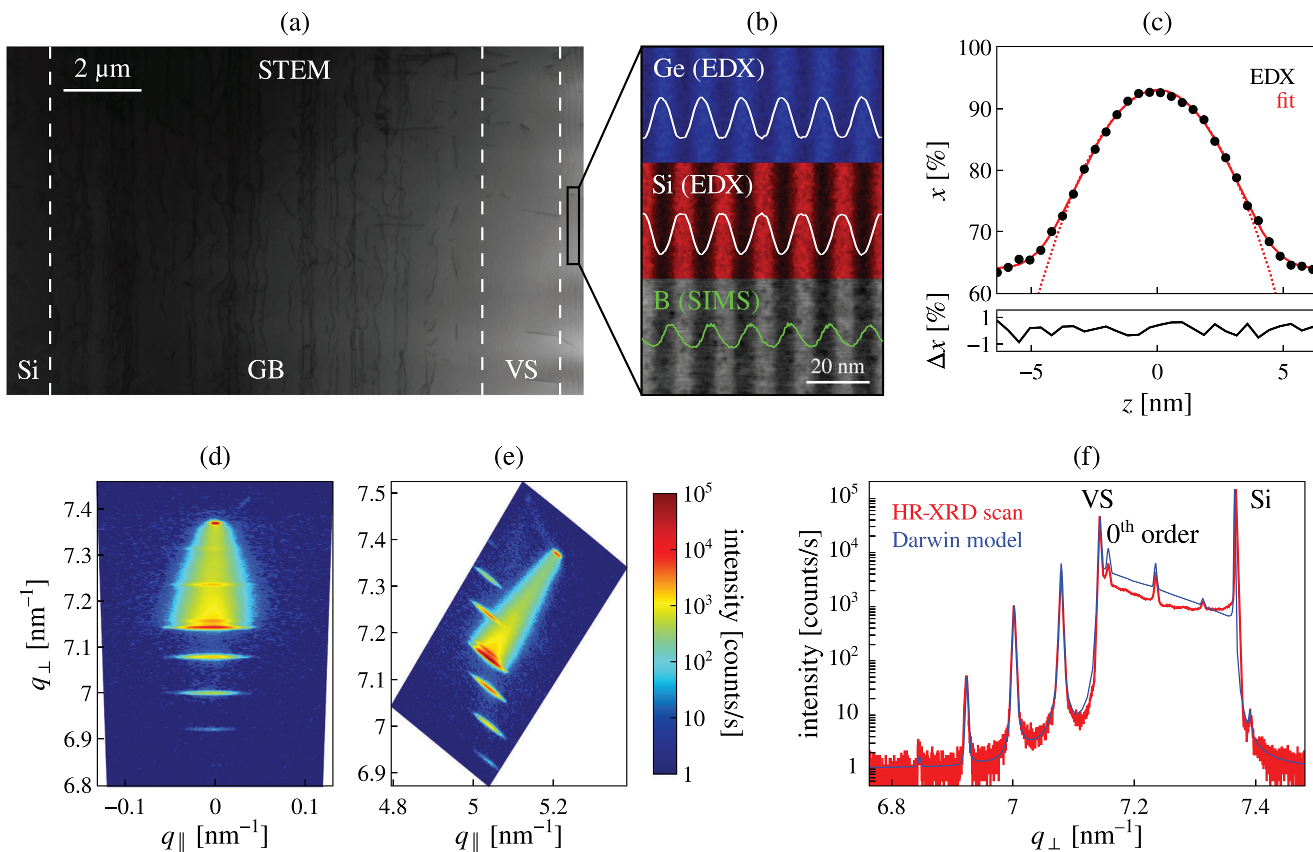

Figure 2. Structural characterization of sample A. a) STEM image showing the Si substrate, the GB, the VS, and the PQWs. The beneficial effect of the GB can be appreciated as dislocations are reduced across the graded layer, and almost entirely disappear in the VS and in the QWs region. b) Detailed STEM image focusing on the QWs region (bottom panel) and EDX intensity maps of Ge (blue) and Si (red) with the measured compositional profiles (white lines). The boron profile retrieved by SIMS (green line) is also reported. c) Germanium content estimated by EDX measurements compared to the smoothed parabolic profile (continuous red line), which accounts for interdiffusion, and to the ideal parabolic profile (dashed red line); deviations from the smoothed profile are reported in the bottom panel. d) Reciprocal space map around the symmetrical (004) diffraction peaks. e) Reciprocal space map around the asymmetrical (224) diffraction peaks. f) ω-2θ XRD scan (red) and best fitting curve obtained by dynamical Darwin model simulations (blue).

In order to assess the crystalline quality of the heterostructure, high-resolution X-ray diffraction (HR-XRD) measurements, coupled with reciprocal space mapping around the symmetrical (004) and asymmetrical (224) reflections, were performed. Figure 2d,e shows the reciprocal space maps referring to sample A. The substrate and VS diffraction peaks together with a roughly linear intensity profile connecting these two features, which is related to the GB, are clearly distinguishable. Moreover, a number of other satellite peaks can be seen that are ascribed to the QWs. The small FWHM of these peaks and the regular spacing confirm the excellent crystal quality of the heterostructure and its uniformity over relatively large areas. However, the 0th order diffraction peak does not perfectly overlap with the one of the VS, suggesting that the average germanium content in the QWs is not exactly matched to the VS. Specifically, the VS composition is around 77.5% while the average composition of the QWs is about 75.5%. The same considerations apply to the ω-2θ XRD scan that is reported in Figure 2f. As HR-XRD measurements are more sensitive to the average composition of the heterostructure than to the actual shape of the compositional profile, the STEM-EDX profile was used as input for the dynamical Darwin model simulation, as implemented by the xrayutilities package,[24,25] and optimized by varying the minimum and maximum concentrations to fit the experimental XRD rocking curve, ultimately achieving a good agreement with concentrations of 59% in the barriers and 93.5% at the center of the wells.

The boron concentration in the QWs region was monitored by SIMS. The corresponding profile is shown in Figure 2b. Even though, according to the growth protocol, boron dopants should exclusively be present at the center of each QW, a baseline of around 2×10^{17} cm^{-3} is observed. Moreover, the concentration is periodically modulated with maxima around 2×10^{18} cm^{-3} whose position, however, does not exactly correspond to the QWs center. Nevertheless, the active dose cannot be directly inferred from these measurements as a non-trivial evolution with temperature might be expected: on the one hand, the effective transfer of all the carriers inside the wells cannot be assumed a priori in semiconductor heterostructures[26] and, on the other hand, temperature plays a key role in dopants ionization.[27] For these reasons, the active carrier concentration was extracted from the optical characterization of ISB transitions.

© 2025 The Author(s). Advanced Optical Materials published by Wiley-VCH GmbH
21951071, 0, Downloaded from https://advanced.onlinelibrary.wiley.com/doi/10.1002/adom.202503060 by POLITECNICO DI MILANO, Wiley Online Library on [09/01/2026]. See the Terms and Conditions (https://onlinelibrary.wiley.com/terms-and-conditions) on Wiley Online Library for rules of use; OA articles are governed by the applicable Creative Commons License

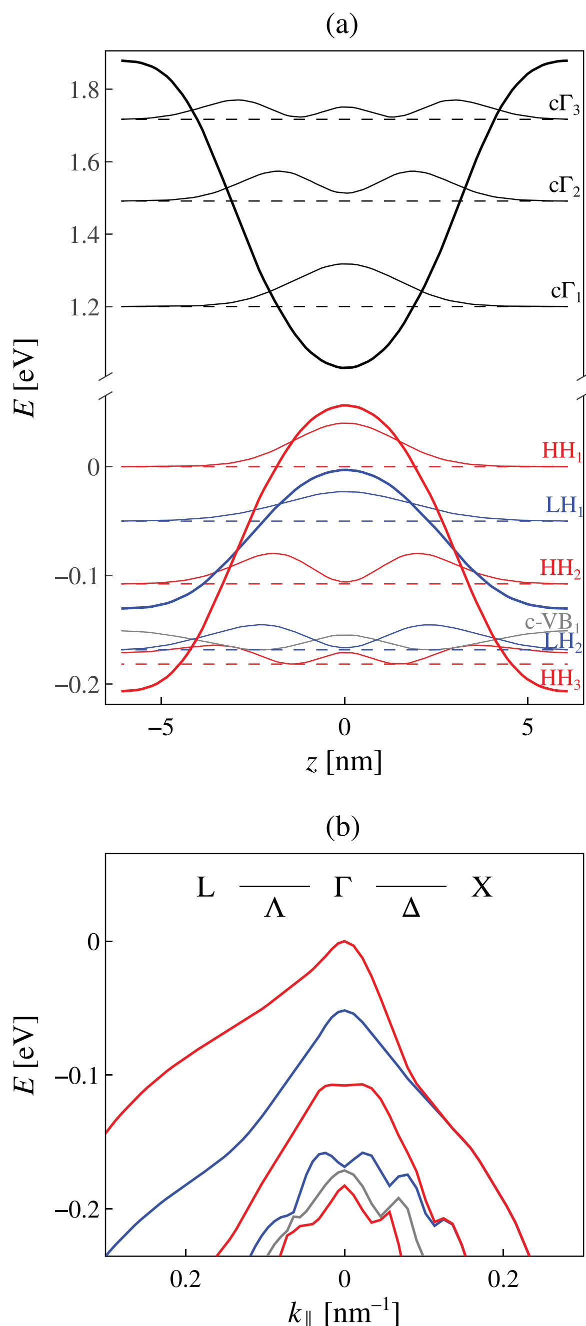

Figure 3. Calculated electronic band structure of the investigated PQWs. a) Γ-point band edge profiles for the valence (HH, LH) and the conduction (cΓ) band and associated squared wavefunctions calculated at 300 K. b) In-plane valence-subbands dispersion along the Λ and Δ high-symmetry directions.

4. Band Structure Calculation

The conduction- and valence-band edge profiles at Γ calculated at 300 K are shown in **Figure 3a**, together with the squared moduli of the wavefunctions associated with the main electronic states. In the conduction band, three confined energy levels exist at Γ which, however, are not equally spaced because of the finite height of the barrier. In the valence band, instead, the situation is complicated by the interplay between HH and LH states. The HH band hosts three confined energy levels, with the first and second excited HH subbands separated by 108 and 181 meV from the ground state HH_1, respectively. The LH band confines a single level, lying around 50 meV below HH_1 while a further level (LH_2), exhibiting LH character, is present above the top of the LH barrier and is almost degenerate with an unbound level (c-VB_1). As the energy separation between the HH_1 and LH_1 states is larger than the thermal energy, the ground state is essentially the only populated level, even at room temperature. The in-plane band structure dispersion of the valence-subbands along the Λ and Δ high-symmetry directions is reported in Figure 3b.

5. Optical Characterization

The optical response of the heterostructures was investigated both in the MIR, i.e., between 100 and 250 meV (between 5 and 12.5 μm wavelength), and in the near-infrared and visible spectral ranges, i.e., between 1.1 and 1.7 eV (between 0.7 and 1.1 μm wavelength), to probe both ISB and interband transitions involving the confined energy levels.

5.1. Interband Characterization

PR spectroscopy was employed to study interband optical transitions at room temperature.[28] **Figure 4** shows the PR spectrum of sample B and the best fitting curve as well as the individual contributions. In order to satisfactorily reproduce the experimental data, at least five different spectral features must be considered.

In infinite square QWs only interband transitions that couple initial and final states whose envelope functions share the same parity are allowed. In finite QWs other transitions become allowed but those fulfilling the parity selection rule remain dominant.[29] Hence, the first three features can be assigned to interband transitions involving the fundamental levels of the HH, LH, SO and cΓ bands, i.e., HH_1-cΓ_1, LH_1-cΓ_1, and SO_1-cΓ_1. Two further features are present at higher energy that are attributed

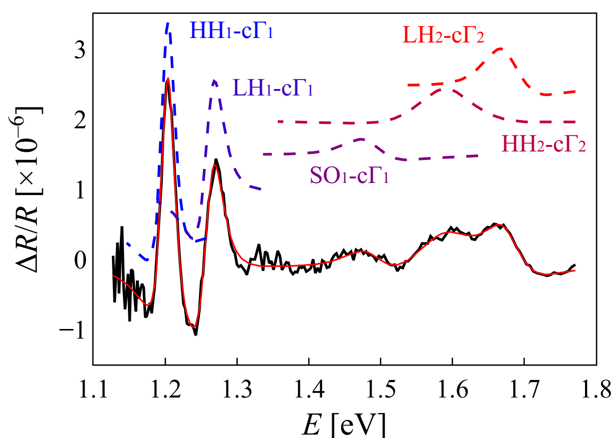

Figure 4. Room-temperature PR spectrum of sample B and best fitting curve. The individual contributions to the total PR spectrum are also shown.

© 2025 The Author(s). Advanced Optical Materials published by Wiley-VCH GmbH

21951071, 0, Downloaded from https://advanced.onlinelibrary.wiley.com/doi/10.1002/adom.202503060 by POLITECNICO DI MILANO, Wiley Online Library on [09/01/2026]. See the Terms and Conditions (https://onlinelibrary.wiley.com/terms-and-conditions) on Wiley Online Library for rules of use; OA articles are governed by the applicable Creative Commons License

Table 2. Experimental and theoretical transition energies of the main interband optical transitions that can be observed in the PR spectra of Figure 5.

Optical transition	Transition energy [eV]	
	Experiment	Calculation
HH_1-$c\Gamma_1$	1.202	1.199
LH_1-$c\Gamma_1$	1.261	1.249
SO_1-$c\Gamma_1$	1.487	1.462
HH_2-$c\Gamma_2$	1.599	1.599
LH_2-$c\Gamma_2$	1.677	1.659

to the HH_2-$c\Gamma_2$ and LH_2-$c\Gamma_2$ transitions. **Table 2** summarizes the resonant energy of these five features together with the corresponding theoretical value, calculated as the energy separating the levels involved in each transition. Comparing the experimental transition energies with the results of the numerical calculations, an excellent agreement is found, thereby confirming the reliability of the theoretical description.

5.2. Intersubband Characterization

Fourier-transform infrared (FTIR) spectroscopy was employed to study the MIR optical response of the heterostructures. The acquisition of dichroic transmission spectra with two perpendicular linear polarizations, in a single-pass waveguide geometry with metal coating on the sample surface, allows for the calculation of the experimental TM-polarized 2D absorption coefficients reported in **Figure 5**. To investigate the temperature dependence of ISB transitions, spectra were acquired at different temperatures, ranging from 10 to 300 K.

Figure 5a shows the experimental absorption spectra of sample C. At all temperatures, the dominant absorption peak is found at energies around 120 meV, corresponding to HH_1-HH_2 ISB transitions. At low temperature, this peak is symmetric and exhibits a narrow absorption line with FWHM of 13 meV, i.e., around 11% of the resonance energy. As temperature increases, the peak becomes weaker, slightly asymmetric and broader, with the FWHM never exceeding 18 meV, even at room temperature. Moreover, the peak position redshifts by a few meV with temperature. Although this shift should not be present in PQWs, it could be tentatively ascribed to the Coulomb potential due to the presence of ionized acceptors in the wells, to the non-parabolic dispersion of the valence band, to the smoothening of the parabolic profile when approaching the barriers, or to a combination of all these effects.

The spectra of sample D, shown in Figure 5b, are similar to the ones of Figure 5a apart from the stronger absorption due to the increased doping level. Similar considerations apply concerning the shape and evolution with temperature of the main absorption line. Interestingly, the low-temperature broadening is around 14.5 meV and it increases with temperature up to around 20 meV. Despite the different doping, these values are

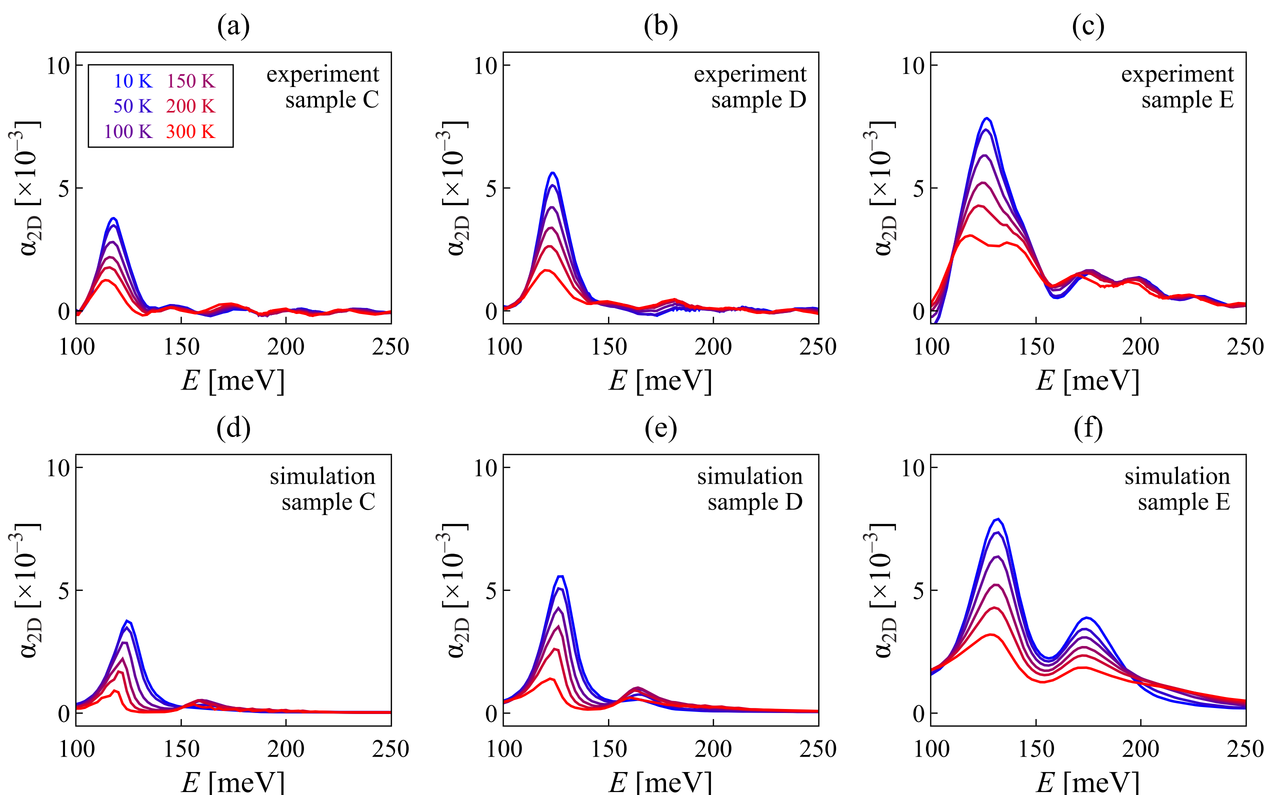

Figure 5. Temperature-dependent TM-polarized 2D absorption coefficient of PQWs measured by FTIR dichroic transmission spectroscopy. Experimental absorption spectra of a) sample C, b) sample D, and c) sample E. Theoretical absorption spectra of d) sample C, e) sample D, and f) sample E, calculated starting from the band structure shown in Figure 3 and considering the experimental sheet hole density.

© 2025 The Author(s). Advanced Optical Materials published by Wiley-VCH GmbH

21951071, 0, Downloaded from https://advanced.onlinelibrary.wiley.com/doi/10.1002/adom.202503060 by POLITECNICO DI MILANO, Wiley Online Library on [09/01/2026]. See the Terms and Conditions (https://onlinelibrary.wiley.com/terms-and-conditions) on Wiley Online Library for rules of use; OA articles are governed by the applicable Creative Commons License

comparable to those observed in sample C, suggesting that scattering by ionized impurities is not the dominant broadening mechanism limiting the linewidth of the resonances, as it does not scale significantly with doping. Therefore, other broadening mechanisms, such as alloy scattering or inhomogeneous broadening, seem to prevail.[30]

The absorption spectra of sample E are shown in Figure 5c. With respect to samples C and D, the main absorption line around 120 meV gets more structured and satellite features emerge at higher energy, i.e., between 160 and 230 meV. This complex behavior is attributed to the non-parabolic dispersion of the electronic states in the valence band as can be seen in Figure 3b. Indeed, the sheet hole density that can be estimated from the spectra at 10 K is approximately 3.6×10^{12} cm^{-2}, meaning that the carriers occupy, even at cryogenic temperature, a large region around Γ where the parabolic approximation no longer holds.

To compare the experimental results with the theoretical predictions, the absorption spectra have to be calculated considering the respective sheet hole density, which can be estimated by integrating the experimental 2D absorption coefficient.[31] Figure 5d–f displays the calculated spectra that already include many-body corrections such as depolarization and exchange-correlation shifts.[31] The experimental curves of samples C and D are well reproduced by the theoretical ones. The calculated spectra also predict the presence of a weak feature around 160 meV, associated with HH_1-LH_2 ISB transitions, which is barely visible in the experimental data, possibly because of the overlap with periodic Fabry-Pèrot interference fringes. The experimental spectra of sample E suggest a splitting of the fundamental absorption peak with increasing temperature, which is much less pronounced in simulations that only feature a single asymmetric peak, due to non-parabolicity and corresponding to HH_1-HH_2 transitions: therefore, the apparent splitting is also partially ascribed to the superimposed Fabry-Pèrot oscillations. Moreover, higher-energy absorption features are also predicted by the calculations. At low temperature, this tail is mainly due to HH_1-LH_2 transitions but, with increasing temperature, ISB transitions involving the c-VB_1 state gain oscillator strength becoming more and more important.

To summarize, relatively intense and temperature-stable ISB transitions can be achieved in the investigated *p*-type SiGe PQWs up to room temperature, also at high doping levels, i.e., up to around 10^{12} cm^{-2}, despite band non-parabolicity effects. This peculiar property makes these or similar PQWs an ideal material platform for the investigation of polaritonic effects in the strong light-matter coupling regime. When multiple QWs are enclosed in a microcavity, ISB transitions interact with resonant photonic modes of the cavity and the degeneracy is lifted, giving rise to quasi-particles known as ISB polaritons. Assuming a perfect overlap between the photonic mode and the heterostructure, the coupling strength is related to the minimum splitting ΔE separating the two polaritonic branches, which is given by[32]

$$\Delta E = \hbar \sqrt{f \frac{n_{2D} e^2}{m^* \varepsilon_0 \varepsilon_\infty L_p}} \quad (1)$$

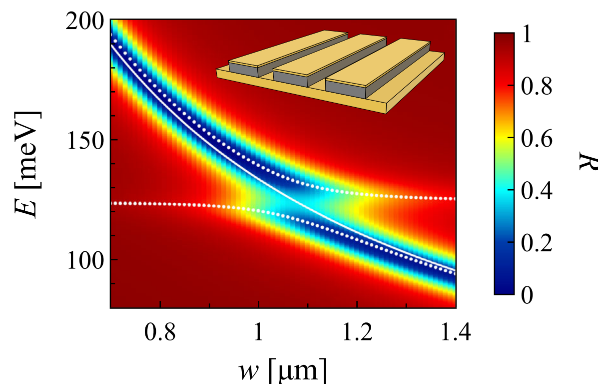

Figure 6. Simulated reflectivity of metal–insulator–metal microcavities in the strong coupling regime where two polaritonic branches can be clearly distinguished. The polaritonic (dashed lines) and bare cavity (solid line) dispersions are also shown in white.

where f is the oscillator strength, n_{2D} is the sheet hole density, m^* is the effective mass of the confined carriers, ε_∞ is the average high-frequency permittivity of the heterostructure and L_p is the period of the QWs. Considering the heterostructure investigated in the present work and the doping levels observed in sample D, a splitting of around 17 meV is estimated at 10 K. To confirm this result, finite-difference time-domain (FDTD) simulations were used to study the interaction of the ISB electronic excitation with the photonic modes sustained by a periodic array of 150 nm-thick etched metal-insulator-metal microcavities featuring top metallic stripes. In the simulations, the polaritonic splitting was monitored through normal-incidence reflectivity while sweeping the stripe width between 0.7 and 1.4 μm, at a fixed periodicity of 2 μm, to tune the spectral position of the microcavity mode. As shown in **Figure 6**, when the cavity mode becomes resonant with the ISB transition, two polaritonic branches, associated with mixed light-matter states, emerge featuring the anti-crossing behaviour typical of the strong coupling regime. Specifically, a polaritonic splitting of approximately 16 meV is obtained, which is slightly lower than the theoretical value, due to the non-perfect overlap of the photonic mode with the heterostructure. Notably, this splitting exceeds both the ISB transition linewidth, extracted from the dichroic spectra, and the photonic mode linewidth, thus enabling the observation of the two polaritons.

6. Conclusion

In this work we demonstrated the design, growth, and characterization of continuously-graded Ge-rich SiGe PQWs, grown by LEPECVD on Si substrates, which exhibit ISB transitions in the MIR spectral range near 120 meV. Through detailed structural analysis using STEM, EDX, SIMS, and HR-XRD, we confirmed that the parabolic shape is preserved in the well region, despite the unavoidable entropic interdiffusion. A strong and stable TM-polarized absorption feature was observed by FTIR spectroscopy up to room temperature at moderate- to high-doping levels, i.e., up to around 10^{12} cm^{-2}. When the doping level is further increased, however, band non-parabolicity effects prevail, and the absorption spectrum becomes more structured. The results of advanced tight-binding calculations, including many-body effects,

© 2025 The Author(s). Advanced Optical Materials published by Wiley-VCH GmbH

21951071, 0, Downloaded from https://advanced.onlinelibrary.wiley.com/doi/10.1002/adom.202503060 by POLITECNICO DI MILANO, Wiley Online Library on [09/01/2026]. See the Terms and Conditions (https://onlinelibrary.wiley.com/terms-and-conditions) on Wiley Online Library for rules of use; OA articles are governed by the applicable Creative Commons License

excellently agree with the experimental data, therefore confirming the reliability of these simulations as a design tool for advanced SiGe heterostructures. In conclusion, this study provides guidelines for the design and realization of SiGe PQWs that can be carefully optimized to develop a robust and tunable material platform for the implementation of Si-compatible ISB-based MIR optoelectronic devices.

7. Experimental Section

Growth: The samples were deposited by LEPECVD on 100 mm (001)-oriented silicon wafers (resistivity 1 ÷ 10 Ω cm) using silane (SiH_4), germane (GeH_4), and diborane (B_2H_6) as precursor gases for silicon, germanium and boron, respectively. The first part of the stack was grown at a rate of 5 nm s^{-1} while decreasing the temperature from 720 to 550 °C for the GB and keeping it fixed at 550 °C for the VS. To achieve fine control over the compositional profile and minimize interdiffusion, the QWs were grown at a growth rate of 0.15 nm s^{-1} and a temperature of 400 °C.

Structural Characterization: STEM measurements were performed using a FEI Titan microscope operating at 200 kV equipped with aberration-corrected magnetic lenses to obtain electron probes with a diameter in the range of 1 ÷ 2 Å and a beam current of 200 pA. A high-angle annular dark field detector was employed to acquire the STEM images. Samples for STEM were prepared using the conventional method of grinding, polishing, and argon ion thinning. EDX measurements were performed using a FEI Tecnai Osiris operated at 200 kV in scanning transmission electron microscopy mode. Time of flight SIMS V from IONTOF was also employed for the measurement of the compositional profiles. The depth profiles were acquired using a Cs^+ ion beam of 0.5 ÷ 1 keV. HR-XRD measurements were performed with a PANanalytical X'Pert PRO MRD diffractometer at room temperature.

Theoretical Calculations: The electronic band structure and wavefunctions were calculated by a semiempirical first-neighbor $sp^3d^5\sigma^*$ tight-binding Hamiltonian model[33–35] that accounts for spin-orbit interaction, thus allowing for a reliable description of the strong non-parabolicity and band-mixing effects typical of the valence band. The self-energy and hopping parameters were taken from Boykin et al.[36] The theoretical ISB absorption spectra were calculated by means of Fermi's golden rule sampling the Brillouin zone and using the experimental sheet hole carrier densities. Furthermore, a phenomenological Lorentzian line broadening was used. Many-body effects were also accounted for by applying the model proposed by Bandara et al.[37] for the exchange-correlation shift and by Ando et al.[38] for the depolarization shift.

Photoreflectance: The PR setup consists of a broadband halogen lamp and a Digikröm CM110 1/8-meter monochromator which produce a monochromatic probe beam with spectral resolution of around 10 nm; the probe beam is then focused onto the sample at an incident angle of 45° and the reflected radiation is collected by a Si amplified photodetector. The reflectivity is periodically modulated by a laser beam emitting 20 mW at 485 nm and mechanically chopped at 971 Hz, which illuminates the surface of the sample at normal incidence. The reflectivity variation ΔR induced by the laser is obtained by conventional lock-in detection and the PR signal is calculated as $\Delta R/R$, with R being the unmodulated reflectivity. The standard third-derivative lineshape,[39,40] usually employed to describe excitonic transitions in PR spectra, was used to fit the experimental data and extract the transition energies.

FTIR Characterization: The dichroic transmission spectra were acquired with a Bruker Invenio FTIR spectrometer equipped with an Oxford OptistatDry BLV closed-circuit helium cryostat, a broadband linear polarizer, and a liquid-N_2-cooled HgCdTe photodetector covering the spectral region between 100 and 250 meV. After having deposited a metallic bilayer (Ti/Au 10/150 nm) on top of the QWs, the samples were shaped in the 2 mm-long single-pass prism-like waveguide geometry with 70° facets to favor the excitation of TM-polarized ISB transitions.[41] The dichroic transmission spectra were calculated as the ratio between the transmission spectra acquired for light oscillating parallel (TM) and perpendicular (TE) to the growth direction of the heterostructures. Starting from the dichroic transmission spectrum, the 2D absorption coefficient can be readily derived as[31]

$$\alpha_{2D} = -\frac{\ln\left(I_{TM}/I_{TE}\right)}{CMN}\frac{\cos\theta}{\sin^2\theta} \tag{2}$$

where C is the field enhancement provided by the metallic layer, $M = 2$ is twice the number of reflections at the heterostructure–metal interface, $N = 20$ is the number of QWs, and $\theta = 57°$ is the propagation angle with respect to the growth direction in the QW region. The frequency-dependent enhancement factor C was evaluated by spatially averaging the standing-wave electric field intensity within the heterostructure. The sheet carrier density n_{2D} in the wells was obtained from α_{2D} using the relation[31]

$$n_{2D} = \frac{2m^* c\varepsilon_0\sqrt{\varepsilon_\infty}}{\pi e^2\hbar}\frac{1}{f}\int \alpha_{2D}(E)\,dE \tag{3}$$

where m^* is the carrier effective mass, ε_∞ is the average permittivity of the heterostructure and f is the oscillator strength, here set to 1. In particular, the HH effective mass $m^* = 0.33\ m_e$ of bulk Ge was used, since no major variations are anticipated when considering confinement and strain effects. The heterostructure permittivity was calculated by linear interpolation of the permittivities of Ge and Si, obtaining $\varepsilon_\infty = 15.2$.

FDTD Simulations: 2D FDTD simulations of etched stripe microcavities were performed using Ansys Lumerical. The normal-incidence reflectivity was measured under plane-wave illumination using a frequency-domain power monitor. The simulation environment includes the bottom mirror, the QWs, the top metallic stripe, the plane-wave source, and the field monitor. The tabulated optical constants of gold[42] were used to describe the response of the metallic regions. The optical properties of the QWs were modeled by a diagonal dielectric tensor with constant permittivity along the in-plane directions and a Lorentzian term describing the ISB transition along the growth direction, whose parameters were retrieved from the FTIR dichroic transmission spectra. Periodic boundary conditions were applied along one in-plane direction, effectively replicating the unit cell infinitely, while the stripes extend indefinitely along the orthogonal in-plane direction. Along the vertical direction, perfectly matched layer boundary conditions were used. To couple to the microcavities, the impinging electric field must oscillate perpendicularly to the stripes. Therefore, only half of the unit cell was simulated, exploiting the anti-symmetric nature of the electric field with respect to the vertical axis to reconstruct the other half.

Acknowledgements

The authors acknowledge financial support from the Italian Ministry of Education, University and Research (MIUR) through the project PRIN 2020 "RETINA" prot. 2020P8WE5S_004. This research has also received funding from the European Union – Next Generation EU – "Fondo PRIN 2022" – germanium Quantum wells for SENSing in the midinfrarEd – id: 2022X5CXTJ – CUP: D53D23002450001. The authors acknowledge the National Centre for HPC, Big Data and Quantum Computing, under the National Recovery and Resilience Plan (NRRP), Mission 4 Component 2 Investment 1.4 CUP I53C22000690001 funded from the European Union, NextGenerationEU. This research has been co-funded by the European Union (ERC, Electrophot, 101097569). Views and opinions expressed are however those of the author(s) only and do not necessarily reflect those of the European Union or the European Research Council. Neither the European Union nor the granting authority can be held responsible for them.

Open access publishing facilitated by Politecnico di Milano, as part of the Wiley - CRUI-CARE agreement.

Conflict of Interest

The authors declare no conflict of interest.

© 2025 The Author(s). Advanced Optical Materials published by Wiley-VCH GmbH

21951071, 0, Downloaded from https://advanced.onlinelibrary.wiley.com/doi/10.1002/adom.202503060 by POLITECNICO DI MILANO, Wiley Online Library on [09/01/2026]. See the Terms and Conditions (https://onlinelibrary.wiley.com/terms-and-conditions) on Wiley Online Library for rules of use; OA articles are governed by the applicable Creative Commons License

Data Availability Statement

The data that support the findings of this study are openly available in [Zenodo] at [https://doi.org/10.5281/zenodo.17122807], reference number [17122807].

Keywords

intersubband, mid-infrared photonics, parabolic quantum wells, silicon-germanium

Received: September 16, 2025
Revised: November 22, 2025
Published online:

[1] Y.-C. Chang, P. Wägli, V. Paeder, A. Homsy, L. Hvozdara, P. van der Wal, J. Di Francesco, N. F. de Rooij, H. P. Herzig, *Lab Chip* **2012**, *12*, 3020.
[2] F. Ottonello-Briano, C. Errando-Herranz, H. Rödjegård, H. Martin, H. Sohlström, K. B. Gylfason, *Opt. Lett.* **2020**, *45*, 109.
[3] H. D. Yallew, M. Vlk, A. Datta, S. Alberti, R. A. Zakoldaev, J. Høvik, A. Aksnes, J. Jágerská, *ACS Photonics* **2023**, *10*, 4282.
[4] H. Schneider, M. Walther, C. Schönbein, R. Rehm, J. Fleissner, W. Pletschen, J. Braunstein, P. Koidl, G. Weimann, J. Ziegler, W. Cabanski, *Physica E* **2000**, *7*, 101.
[5] D. Marris-Morini, V. Vakarin, J. M. Ramirez, Q. Liu, A. Ballabio, J. Frigerio, M. Montesinos, C. Alonso-Ramos, X. Le Roux, S. Serna, D. Benedikovic, D. Chrastina, L. Vivien, G. Isella, *Nanophotonics* **2018**, *7*, 1781.
[6] M. Montanari, C. Ciano, L. Persichetti, C. Corley, L. Baldassarre, M. Ortolani, L. Di Gaspare, G. Capellini, D. Stark, G. Scalari, M. Virgilio, M. De Seta, *Appl. Phys. Lett.* **2021**, *19*, 118.
[7] E. Campagna, E. Talamas Simola, T. Venanzi, F. Berkmann, C. Corley-Wiciak, G. Nicotra, L. Baldassarre, G. Capellini, L. Di Gaspare, M. Virgilio, M. Ortolani, M. De Seta, *Nanophotonics* **2024**, *13*, 1793.
[8] M. Helm, P. Kruck, T. Fromherz, A. Weichselbaum, M. Seto, G. Bauer, Z. Moussa, P. Boucaud, F. H. Julien, J.-M. Lourtioz, J. F. Nützel, G. Abstreiter, *Thin Solid Films* **1997**, *294*, 330.
[9] T. Fromherz, M. Meduňa, G. Bauer, A. Borak, C. V. Falub, S. Tsujino, H. Sigg, D. Grützmacher, *J. Appl. Phys.* **2005**, *98*, 044501.
[10] J. Frigerio, A. Ballabio, M. Ortolani, M. Virgilio, *Opt. Express* **2018**, *26*, 31861.
[11] A. Barzaghi, V. Falcone, S. Calcaterra, D. Marris-Morini, M. Virgilio, J. Frigerio, *Opt. Express* **2022**, *30*, 46710.
[12] M. Faverzani, S. Calcaterra, P. Biagioni, J. Frigerio, *Nanophotonics* **2024**, *13*, 1693.
[13] F. Berkmann, T. Venanzi, L. Baldassarre, E. Campagna, E. Talamas Simola, L. Di Gaspare, C. Corley-Wiciak, G. Capellini, G. Nicotra, G. Sfuncia, A. Notargiacomo, E. Giovine, S. Cibella, M. Virgilio, G. Scalari, M. De Seta, M. Ortolani, *ACS Photonics* **2024**, *11*, 2776.
[14] L. Brey, N. F. Johnson, B. I. Halperin, *Phys. Rev. B* **1989**, *40*, 10647.
[15] R. P. G. Karunasiri, K. L. Wang, *Superlatt. Microstruct.* **1988**, *4*, 661.
[16] M. Geiser, F. Castellano, G. Scalari, M. Beck, L. Nevou, J. Faist, *Phys. Rev. Lett.* **2012**, *108*, 106402.
[17] C. Deimert, Z. R. Wasilewski, *J. Cryst. Growth* **2019**, *514*, 103.
[18] C. Deimert, P. Goulain, J.-M. Manceau, W. Pasek, T. Yoon, A. Bousseksou, N. Y. Kim, R. Colombelli, Z. R. Wasilewski, *Phys. Rev. Lett.* **2020**, *125*, 097403.
[19] A. Ballabio, J. Frigerio, S. Firoozabadi, D. Chrastina, A. Beyer, K. Volz, G. Isella, *J. Phys. D: Appl. Phys.* **2019**, *52*, 415105.
[20] P. Goulain, M. Jeannin, C. Deimert, T. Blaikie, S. Pirotta, A. Wright, A. De Vetter, M. Mičica, S. Dhillon, Z. R. Wasilewski, R. Colombelli, J.-M. Manceau, *Appl. Phys. Lett.* **2024**, *125*, 153503.
[21] G. Isella, D. Chrastina, B. Rössner, T. Hackbarth, H. J. Herzog, U. König, H. von Känel, *Solid-State Electron.* **2004**, *48*, 1317.
[22] S. Cecchi, E. Gatti, D. Chrastina, J. Frigerio, E. Müller Gubler, D. J. Paul, M. Guzzi, G. Isella, *J. Appl. Phys.* **2014**, *115*, 093502.
[23] F. Schaffler, in *Properties of Advanced Semiconductor Materials GaN, AlN, InN, BN, SiC, SiGe*, (Eds: M. E. Levinshtein, S. L. Rumyantsev, M. S. Shur), John Wiley & Sons, Inc., New York **2001**, pp. 149-188.
[24] C. G. Darwin, *Philos. Mag.* **1914**, *27*, 315.
[25] D. Kriegner, E. Wintersberger, J. Stangl, *J. Appl. Crystallogr.* **2013**, *46*, 1162.
[26] E. Campagna, E. Talamas Simola, L. Di Gaspare, D. Marian, M. H. Zoellner, F. Berkmann, L. Baldassarre, M. Ortolani, G. Capellini, M. Virgilio, M. De Seta, *APL Mater.* **2025**, *13*, 061112.
[27] S. Calcaterra, M. Faverzani, D. Impelluso, D. Chrastina, R. Giani, L. Anzi, J. H. Bae, C. Tassi, D. Buca, P. Biagioni, G. Isella, M. Virgilio, J. Frigerio, *Phys. Rev. B* **2025**, *112*, 045429.
[28] C. Zucchetti, A. Ballabio, D. Chrastina, S. Cecchi, M. Finazzi, M. Virgilio, G. Isella, F. Bottegoni, *Phys. Rev. B* **2020**, *101*, 115408.
[29] G. Bastard, *Wave Mechanics Applied to Semiconductor Heterostructures*, Les Editions de Physique, Les Ulis, France **1988**, 247.
[30] C. Ndebeka-Bandou, F. Carosella, R. Ferreira, A. Wacker, G. Bastard, *Semicond. Sci. Technol.* **2014**, *29*, 023001.
[31] E. R. Weber, R. K. Willardson, H. C. Liu, F. Capasso, *Intersubband Transitions in Quantum Wells*, Academic Press, Cambridge, UK **1999**.
[32] Y. Todorov, C. Sirtori, *Phys. Rev. B* **2012**, *85*, 045304.
[33] M. Virgilio, G. Grosso, *J. App. Phys.* **2006**, *100*, 093506.
[34] M. Virgilio, G. Grosso, *Phys. Rev. B* **2009**, *79*, 165310.
[35] G. Pizzi, M. Virgilio, G. Grosso, *Nanotechnology* **2010**, *21*, 055202.
[36] T. B. Boykin, G. Klimeck, F. Oyafuso, *Phys. Rev. B* **2004**, *69*, 115201.
[37] K. M. S. V. Bandara, D. D. Coon, O. Byungsung, Y. F. Lin, M. H. Francombe, *Appl. Phys. Lett.* **1988**, *53*, 1931.
[38] T. Ando, A. B. Fowler, F. Stern, *Rev. Mod. Phys.* **1982**, *54*, 437.
[39] D. E. Aspnes, *Surf. Sci.* **1973**, *37*, 418.
[40] F. H. Pollak, H. Shen, *Mater. Sci. Eng. Rep.* **1993**, *10*, xv.
[41] M. J. Kane, M. T. Emeny, N. Apsley, C. R. Whitehouse, D. Lee, *Semicond. Sci. Technol.* **1988**, *3*, 722.
[42] E. D. Palik, *Handbook of optical constants of solids*, Vol. *3*. Academic press, Cambridge, UK **1998**.

© 2025 The Author(s). Advanced Optical Materials published by Wiley-VCH GmbH

21951071, 0, Downloaded from https://advanced.onlinelibrary.wiley.com/doi/10.1002/adom.202503060 by POLITECNICO DI MILANO, Wiley Online Library on [09/01/2026]. See the Terms and Conditions (https://onlinelibrary.wiley.com/terms-and-conditions) on Wiley Online Library for rules of use; OA articles are governed by the applicable Creative Commons License